Nonlinear nanomechanical resonators approaching the quantum ground state

Check for updates

C. Samanta[1], S. L. De Bonis[1], C. B. Møller[1], R. Tormo-Queralt [1], W. Yang [1], C. Urgell[1], B. Stamenic[2], B. Thibeault[2], Y. Jin[3], D. A. Czaplewski [4], F. Pistolesi[5] & A. Bachtold [1] ✉

It is an open question whether mechanical resonators can be made nonlinear with vibrations approaching the quantum ground state. This requires the engineering of a mechanical nonlinearity far beyond what has been realized so far. Here we discover a mechanism to boost the Duffing nonlinearity by coupling the vibrations of a nanotube resonator to single-electron tunnelling and by operating the system in the ultrastrong-coupling regime. We find that thermal vibrations become highly nonlinear when lowering the temperature. The average vibration amplitude at the lowest temperature is 13 times the zero-point motion, with approximately 42% of the thermal energy stored in the anharmonic part of the potential. Our work may enable the realization of mechanical Schrödinger cat states, mechanical qubits and quantum simulators emulating the electron–phonon coupling.

Mechanical resonators are perfect linear systems in experiments carried out in the quantum regime. Such devices enable the quantum squeezing of mechanical motion[1-3], quantum backaction-evading measurements[4-6] and entanglement between mechanical resonators[7,8]. Achieving nonlinear vibrations in resonators cooled to the quantum ground state would offer novel prospects for the quantum control of their motion. These include the development of mechanical qubits[9,10] and mechanical Schrödinger cat states[11]. Creating strong nonlinearities near the quantum ground state, with the displacement fluctuations given by the zero-point motion x_{zp}, has so far been out of reach in all mechanical systems explored thus far. Various mechanical resonators have been experimentally cooled to the ground state (Fig. 1, blue stars); however, they become only appreciably nonlinear for vibration amplitudes x_{nl} that are 10^6 times larger than x_{zp}. Small resonators based on nanoscale objects feature comparatively large zero-point motion. Carbon nanotubes are the narrowest resonators with diameters typically between 1 and 3 nm, whereas graphene and semiconductor monolayers are the thinnest membranes, as they are atomically thin. Levitated particles can also be small when they are trapped by a focused laser beam. Despite the large zero-point motion of all these nanoscale resonators, nonlinear effects appear for x_{nl}/x_{zp} ranging from 10^3 to 10^5 (Fig. 1).

The emergence of nonlinearities for large displacements is related to the weak Duffing (or Kerr) constant γ, which enters the restoring force as $F = -m\omega_m^2 x - \gamma x^3$, where m is the mechanical eigenmode mass and ω_m is the resonance frequency. The origin of nonlinearities in mechanical resonators is often related to the nonlinear dependence of stress on the displacement field of the mode[12,13]. Nonlinearities can be engineered using a force field gradient or a two-level system. Although mechanical systems have been operated in large field gradients[14,15] and strongly coupled to two-level systems[16-23], it has not been possible to substantially increase mechanical nonlinearities. The nonlinearity of levitated particles arises from the focused laser beam and is difficult to further enhance. Due to the weak Duffing constant, thermal fluctuations become nonlinear at high temperatures far away from the quantum regime. This occurs at room temperature for levitated particles[24] and even higher temperatures for mechanical resonators[25,26].

Here we demonstrate a new mechanism to boost the vibration nonlinearity by coupling a mechanical resonator to single-electron tunnelling (SET) through a quantum dot in a non-resonant manner. The nature of this coupling creates an increasingly larger vibration nonlinearity on lowering the temperature. Thermal vibrations become

[1]ICFO—Institut De Ciencies Fotoniques, The Barcelona Institute of Science and Technology, Castelldefels, Spain. [2]UCSB Nanofabrication Facility, ECE Department, University of California Santa Barbara, Santa Barbara, CA, USA. [3]C2N, CNRS, Université Paris-Saclay, Palaiseau, France. [4]Center for Nanoscale Materials, Argonne National Laboratory, Argonne, IL, USA. [5]Université de Bordeaux, CNRS, LOMA, UMR 5798, Talence, France. ✉e-mail: adrian.bachtold@icfo.eu
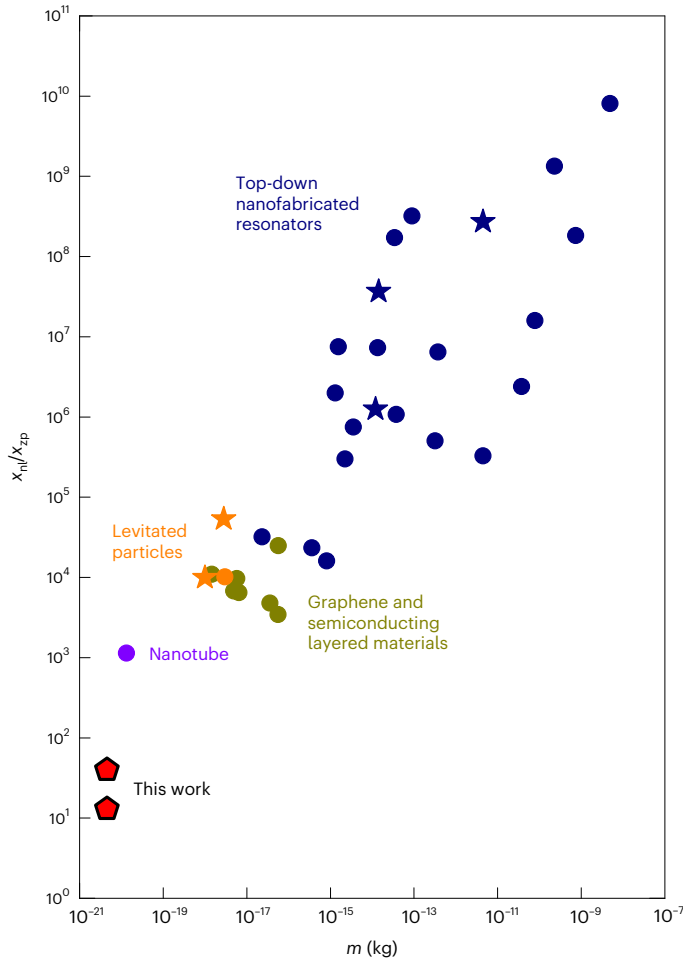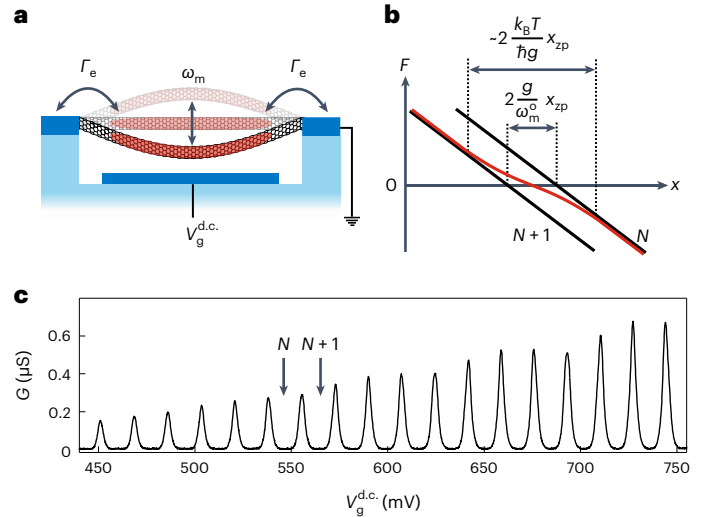
Fig. 1 | Vibration amplitude x_{nl} for which nonlinearities emerge divided by the zero-point motion x_{zp} as a function of the mass of the mechanical eigenmode for a large range of different vibrational systems. Different colours correspond to different types of vibrational system. The stars correspond to systems that have been experimentally cooled to the quantum ground state. Supplementary Fig. 11 indicates the reference for each system. When both displacement and frequency fluctuations are negligible, the effect of Duffing nonlinearity is sizable when $x_{nl}/x_{zp} > (\beta m^2 \omega_m^2 \Gamma_m/\hbar\gamma)^{1/2}$, where $\beta \simeq 3.1$ is a constant; ω_m, the resonance frequency; Γ_m, the mechanical linewidth; and γ, the Duffing constant[12].

Fig. 2 | SET-based nonlinearity. a, Schematic of the nanotube vibrating at ω_m. A quantum dot (highlighted in red) is formed along the suspended nanotube; the total electron tunnelling rate to the two leads is Γ_e. **b,** Origin of the SET-based nonlinearity. The two linear force–displacement curves (shown in black) correspond to the dot filled with either N or $N+1$ electrons; the slope is given by the spring constant $m\omega_m^{o\,2}$ and the two curves are separated by $\Delta x = 2(g/\omega_m^o)x_{zp}$ caused by the force created by one electron tunnelling onto the quantum dot. The force felt by the vibrations is an average of the two black forces weighted by the Fermi–Dirac distribution when $\Gamma_e > \omega_m^o$. The resulting force (red) is nonlinear for vibration displacements smaller than $\sim \frac{k_B T}{\hbar g} x_{zp}$; the reduced slope at zero vibration displacement indicates the decrease in ω_m. **c,** Gate voltage dependence of conductance G of device I at $T = 6$ K.

highly nonlinear at subkelvin temperatures when the average displacement amplitude decreases to $x_{nl} \simeq 13 \times x_{zp}$, with about 42% of the thermal energy stored in the anharmonic part of the potential. Having the nonlinear part of the restoring force comparable with its linear part is extreme for mechanical resonators[27]. This is even more remarkable considering that the thermal vibration amplitude is so close to the zero-point motion.

The device consists of a quantum dot embedded in a vibrating nanotube (Fig. 2a). The nanotube is a small-bandgap semiconductor whose electrochemical potential can be tuned by an underlying gate electrode. The quantum dot is formed using the gate to electrostatically create a p–n tunnel junction at both ends of the suspended nanotube. The quantum dot is operated in the incoherent SET regime, where it behaves as a degenerate two-level system fluctuating between two states with N and $N+1$ electrons. The vibrations are coupled to the electrons in the quantum dot via capacitive coupling between the nanotube and gate electrode. The coupling is described by the Hamiltonian $H = -\hbar g n x/x_{zp}$, where g is the electromechanical coupling, $n = 0, 1$ is the additional electron number in the quantum dot and x_{zp} is the

vibration zero-point motion. In the adiabatic limit, when the electron fluctuation rate is faster than the bare mechanical frequency ($\Gamma_e > \omega_m^o$), the fluctuations result in the nonlinear restoring force given by

$$F_{\text{eff}} = -\left[m\omega_m^{o\,2} - \frac{1}{4x_{zp}^2}\frac{(\hbar g)^2}{k_B T} \right] x - \frac{1}{48 x_{zp}^4}\frac{(\hbar g)^4}{(k_B T)^3} x^3 \qquad (1)$$

for $\Gamma_e < k_B T$ and $x \ll 2k_B T/\hbar g$ and when the electronic two-level system is degenerate (Fig. 2b and Supplementary Equation (31)). A striking aspect of the nonlinearity is its temperature dependence, since the nonlinear Duffing constant substantially increases when reducing the temperature. The vibration potential can even become purely quartic in displacement, since the linear part of the restoring force vanishes[28] at a low temperature when $2k_B T = \hbar g^2/\omega_m^o$. This can be realized for mechanical systems not in their motional ground state ($k_B T > \hbar\omega_m^o$) by operating the system in the ultrastrong-coupling regime when $g > \sqrt{2}\omega_m^o$. Equation (1) also indicates that the measurement of a large decrease in ω_m at a low temperature is a direct indication of strong nonlinearity. A large number of experiments have been carried out where mechanical vibrations are coupled to SET[29–37], but the decrease in ω_m has always been modest.

Carbon nanotube electromechanical resonators (Fig. 2a) are uniquely suited for demonstrating a strong vibration nonlinearity. Its ultralow mass gives rise to a large coupling g, which is directly proportional to $x_{zp} = \sqrt{\hbar/2\omega_m^o m}$. Moreover, high-quality quantum dots can be defined along the nanotube by two p–n tunnel junctions that are controlled by electrostatic means. Figure 2c shows a conductance trace featuring regular peaks associated with SET through the system. The average dot occupation increases by one electron over the gate voltage range where a conductance peak is observed. A voltage smaller than $k_B T/e$ is applied to measure the conductance.
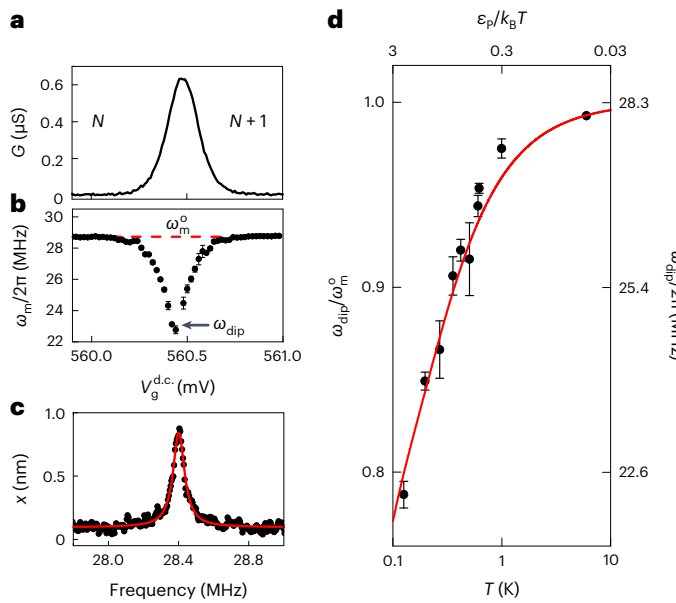
Fig. 3 | Enhanced mechanical vibration nonlinearity at low temperature.
a,b, Conductance (**a**) and mechanical resonance frequency (**b**) as a function of gate voltage $V_g^{d.c.}$ at 300 mK. By counting the number of observed conductance peaks from the nanotube energy gap, we estimate $N = 22$. The red dashed line indicates ω_m^o. **c**, Driven mechanical response measured at 6 K (ref. 40). **d**, Temperature dependence of the resonance frequency. The red solid line is the predicted universal function. The ω_{dip}/ω_m^o reduction is expected to be about 0.75 when the potential is quartic; in this case, although the linear part of F_{eff} is zero, the nonlinear part of F_{eff} combined with thermal vibrations substantially renormalizes ω_m. The confidence-interval error bars in **b** and **d** arise primarily from the standard deviation in ω_m quantified from different driven spectral response measurements.

A large dip in ω_m is observed when setting the system on a conductance peak (Fig. 3a–c) where the electronic two-level system is degenerate. This is consistent with the vibration potential becoming strongly anharmonic. The decrease in ω_m is enhanced at lower temperatures (Fig. 3d), indicating that the high-temperature harmonic potential smoothly evolves into an increasingly anharmonic potential. These data are well reproduced by the universal function predicted for ω_m, which depends only on the ratio $\epsilon_P/k_B T$ (Supplementary Equation (44)); here $\epsilon_P = 2\hbar g^2/\omega_m^o$. In our analysis, we set the temperature of thermal vibrations equal to the temperature of electrons involved in SET, as measured in our previous work[34]; the temperature is measured from the width of the gate voltage of the conductance peaks (Methods and Extended Data Fig. 3). A similar decrease in ω_m was observed in two other devices (Supplementary Section IIE).

These measurements reveal that the system is deep in the ultrastrong-coupling regime. The universal temperature dependence of ω_m enables us to quantify g with accuracy. The largest coupling obtained from measurements at different conductance peaks is $g/2\pi = 0.50 \pm 0.04$ GHz (Fig. 4a, black dots), corresponding to $g/\omega_m^o = 17 \pm 1$. The coupling is consistent with the estimation $g/2\pi = 0.55 \pm 0.18$ GHz obtained from independent measurements (Fig. 4a, purple line) using $g = e(C_g'/C_\Sigma)V_g^{d.c.}/\sqrt{2m\hbar\omega_m^o}$, where m is quantified from driven spectral response measurements and the spatial derivative of the dot-gate capacitance C_g' and total capacitance C_Σ of the quantum dot are obtained from electron transport measurements. Figure 4a–c shows that the device is operated in the ultrastrong-coupling regime ($g > \omega_m^o$) and the adiabatic limit ($\Gamma_e > \omega_m^o$), which are necessary conditions to realize strong vibration anharmonicity. Although it is not directly relevant for this particular implementation, the quantum

cooperativity $4g^2/\Gamma_e\Gamma_{th}$ is above unity over the measured temperature range, where Γ_{th} is the thermal decoherence rate.

We now turn our attention to the driven nonlinear resonant response of the mechanical mode (Fig. 5a,b). The spectral peak is asymmetric for vibration amplitudes as low as $x \simeq 40 \times x_{zp}$. We do not observe the usual hysteresis in the nonlinear response when the driving frequency is swept back and forth. Moreover, the nonlinear resonator has a decreasing responsivity for an increasing drive (Fig. 5c). These data agree with a model that takes into account the strong nonlinearity and thermal fluctuations. The prediction (Fig. 5a,c (red) and Supplementary Fig. 4) is the result of a simultaneous fit over a full set of spectra with different drive amplitudes but with a common set of parameters. The model fully captures the atypical behaviours observed when transitioning from the linear to the nonlinear regime at larger drives. The lack of hysteresis is explained by the low amplitude of driven vibrations compared with the thermal displacement amplitude, an unusual regime for driven nonlinear response measurements[27]. The behaviour of the responsivity arises from the thermal fluctuations that modify the spectral response of the driven nonlinear resonator[27]. From the comparison between data and model, we determine the coupling $g/2\pi = 0.65 \pm 0.22$ GHz. We obtain $g/2\pi = 0.76 \pm 0.20$ GHz from the quadratic dependence of the resonant frequency on the driven
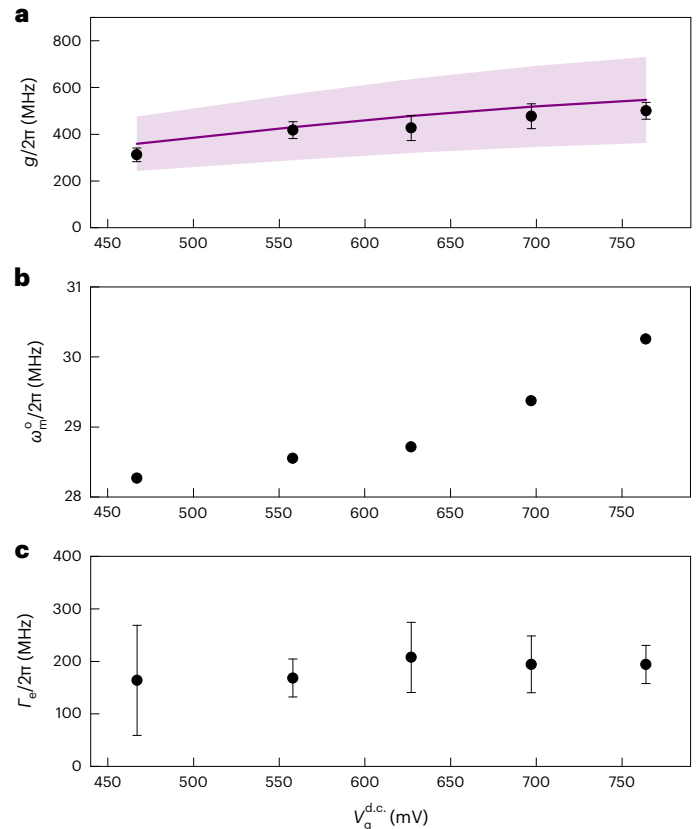
Fig. 4 | Electromechanical resonator in the ultrastrong-coupling regime.
a, Coupling g as a function of $V_g^{d.c.}$. The black data points are obtained from the measured temperature dependence of ω_m. The purple line is estimated from the capacitive force associated with one electron added onto the quantum dot.
b,c, Bare mechanical resonance frequency ω_m^o and electron tunnelling rate Γ_e as a function of $V_g^{d.c.}$. The ω_m^o variation is due to the electrostatically induced stress in the nanotube. We quantify Γ_e from the temperature dependence of the resonance width $\Delta\omega$ in the spectral response measurements. The confidence-interval error bars in **a** (black dots) and **c** primarily arise from the uncertainty in the fit of the measured temperature dependence of ω_m and $\Delta\omega$, respectively, to the predictions of the theory. The confidence interval in the estimation of g shown in **a** (purple-shaded area) mainly originates from the uncertainty in the measurement of the mass.
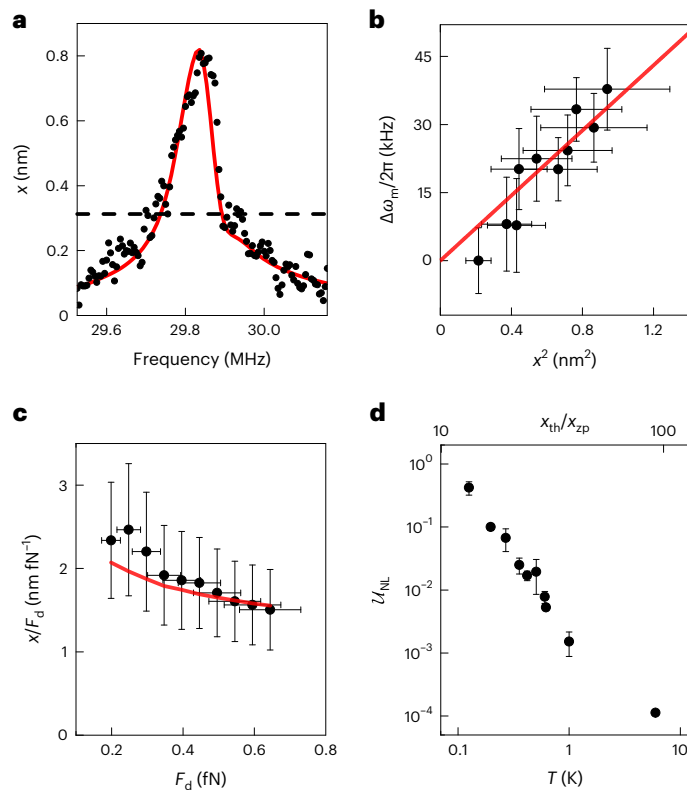
Fig. 5 | Nonlinear mechanical vibrations. The vibrations are measured at $V_g^{d.c.} = 757.2$ mV. **a**, Nonlinear resonant response to the driving force at 6 K. The dashed black line corresponds to $x = 40 \times x_{zp}$. The red line is the simultaneous fit of ten spectra at different drives. The response gets difficult to measure at lower T, since the vibration dissipation is enhanced. **b**, Resonant frequency shift versus the driven vibration amplitude at 6 K. The red line is a linear fit to the data. The driven vibration amplitude is set smaller or comparable with the averaged amplitude of the thermal vibrations x_{th}. **c**, Responsivity x/F_d of the mechanical mode at 6 K, where F_d is the driven force amplitude. The red line is the fit to the theoretical prediction (Supplementary Section IH). **d**, Ratio $\mathcal{U}_{NL}$ between the thermal vibration energy stored in the nonlinear part of the potential and that in the total vibration potential. The confidence-interval error bars in **b** and **c** arise from the uncertainty in the fitting of the spectral response and the determination of the dot-gate separation. The confidence-interval error bars in **d** primarily arises from the uncertainty in the fit of the measured temperature dependence of ω_m to the predictions of the theory.

vibrational amplitude for Duffing resonators (Fig. 5b), which remains approximately valid in the presence of thermal fluctuations provided that the driven vibration amplitude is sufficiently small. These two values of g are consistent with the first two estimates.

The vibrations become strongly nonlinear at a low temperature for vibrations approaching the quantum ground state. Figure 5d shows the fraction of thermal energy stored in the nonlinear part of the vibration potential $\mathcal{U}_{NL} = [\langle U_{eff}(x) \rangle - m\omega_m^2 \langle x^2 \rangle / 2] / \langle U_{eff}(x) \rangle$, where $U_{eff}(x)$ is the total effective vibration potential created by the coupling. The fraction is directly estimated from the measured decrease in ω_m using the theory predictions of the coupled system (Supplementary Section IF). The effect of this nonlinearity on the vibrations becomes increasingly important as the temperature is decreased, since a larger fraction of the thermal energy is stored in the nonlinear part of the potential (Fig. 5d). The fraction $\mathcal{U}_{NL}$ becomes approximately 42% at the lowest measured temperature where the average amplitude of thermal vibrations is $x_{th} \simeq 13 \times x_{zp}$. The large nonlinearity is accompanied by an enhanced damping at a low temperature (Supplementary Section IIB). The damping may be suppressed by electrostatically transforming the embedded single quantum dot into a double quantum dot[33] where

electron tunnelling happens coherently between two dots. This approach preserves both strong mechanical nonlinearities measured in this work[10] and high mechanical quality factors[34,38].

We have demonstrated a mechanism to create a strong mechanical nonlinearity by coupling a mechanical resonator and a two-level system in the ultrastrong-coupling regime. Mechanical resonators endowed with a sizable nonlinearity in the quantum regime enable numerous applications. Novel qubits may be engineered where the information is stored in the mechanical vibrations; such mechanical qubits are expected to inherit the long coherence time of mechanical vibrations and may be used for manipulating quantum information[9,10]. Mechanical 'Schrödinger cat' states—non-classical superpositions of mechanical coherent states—can also be formed[11] with enhanced quantum sensing capabilities in the detection of force and mass. Coupling mechanical vibrations to yet more quantum dots in a linear array may realize an analogue quantum simulator of small-sized quantum materials[39]. Such a simulator could explore the rich physics of strongly correlated systems where the electron–electron repulsion is competing with the electron–phonon interaction.

Online content

Any methods, additional references, Nature Portfolio reporting summaries, source data, extended data, supplementary information, acknowledgements, peer review information; details of author contributions and competing interests; and statements of data and code availability are available at https://doi.org/10.1038/s41567-023-02065-9.

References

1. Pirkkalainen, J.-M., Damskägg, E., Brandt, M., Massel, F. & Sillanpää, M. A. Squeezing of quantum noise of motion in a micromechanical resonator. *Phys. Rev. Lett.* **115**, 243601 (2015).
2. Lecocq, F., Clark, J. B., Simmonds, R. W., Aumentado, J. & Teufel, J. D. Quantum nondemolition measurement of a nonclassical state of a massive object. *Phys. Rev. X* **5**, 041037 (2015).
3. Wollman, E. E. et al. Quantum squeezing of motion in a mechanical resonator. *Science* **349**, 952–955 (2015).
4. Suh, J. et al. Mechanically detecting and avoiding the quantum fluctuations of a microwave field. *Science* **344**, 1262–1265 (2014).
5. Ockeloen-Korppi, C. F. et al. Quantum backaction evading measurement of collective mechanical modes. *Phys. Rev. Lett.* **117**, 140401 (2016).
6. Møller, C. B. et al. Quantum back-action-evading measurement of motion in a negative mass reference frame. *Nature* **547**, 191–195 (2017).
7. Kotler, S. et al. Direct observation of deterministic macroscopic entanglement. *Science* **372**, 622–625 (2021).
8. Wollack, E. A. et al. Quantum state preparation and tomography of entangled mechanical resonators. *Nature* **604**, 463–467 (2022).
9. Rips, S. & Hartmann, M. J. Quantum information processing with nanomechanical qubits. *Phys. Rev. Lett.* **110**, 120503 (2013).
10. Pistolesi, F., Cleland, A. N. & Bachtold, A. Proposal for a nanomechanical qubit. *Phys. Rev. X* **11**, 031027 (2021).
11. Kirchmair, G. et al. Observation of quantum state collapse and revival due to the single-photon Kerr effect. *Nature* **495**, 205–209 (2013).
12. Lifshitz, R. & Cross, M. C. Nonlinear dynamics of nanomechanical and micromechanical resonators. in *Reviews of Nonlinear Dynamics and Complexity* Ch. 1 (John Wiley & Sons, 2008).
13. Postma, H. W. C., Kozinsky, I., Husain, A. & Roukes, M. L. Dynamic range of nanotube- and nanowire-based electromechanical systems. *Appl. Phys. Lett.* **86**, 223105 (2005).
14. Gloppe, A. et al. Bidimensional nano-optomechanics and topological backaction in a non-conservative radiation force field. *Nat. Nanotechnol.* **9**, 920–926 (2014).

15. Unterreithmeier, Q. P., Weig, E. M. & Kotthaus, J. P. Universal transduction scheme for nanomechanical systems based on dielectric forces. *Nature* **458**, 1001–1004 (2009).

16. Kettler, J. et al. Inducing micromechanical motion by optical excitation of a single quantum dot. *Nat. Nanotechnol.* **16**, 283–287 (2021).

17. O'Connell, A. D. et al. Quantum ground state and single-phonon control of a mechanical resonator. *Nature* **464**, 697–703 (2010).

18. Satzinger, K. J. et al. Quantum control of surface acoustic-wave phonons. *Nature* **563**, 661–665 (2018).

19. Chu, Y. et al. Creation and control of multi-phonon Fock states in a bulk acoustic-wave resonator. *Nature* **563**, 666–670 (2018).

20. Arrangoiz-Arriola, P. et al. Resolving the energy levels of a nanomechanical oscillator. *Nature* **571**, 537–540 (2019).

21. LaHaye, M. D., Suh, J., Echternach, P. M., Schwab, K. C. & Roukes, M. L. Nanomechanical measurements of a superconducting qubit. *Nature* **459**, 960–964 (2009).

22. Pirkkalainen, J.-M. et al. Hybrid circuit cavity quantum electrodynamics with a micromechanical resonator. *Nature* **494**, 211–215 (2013).

23. Ma, X., Viennot, J. J., Kotler, S., Teufel, J. D. & Lehnert, K. W. Non-classical energy squeezing of a macroscopic mechanical oscillator. *Nat. Phys.* **17**, 322–326 (2021).

24. Gieseler, J., Novotny, L. & Quidant, R. Thermal nonlinearities in a nanomechanical oscillator. *Nat. Phys.* **9**, 806–810 (2013).

25. Maillet, O. et al. Nonlinear frequency transduction of nano-mechanical Brownian motion. *Phys. Rev. B* **96**, 165434 (2017).

26. Huang, L. et al. Frequency stabilization and noise-induced spectral narrowing in resonators with zero dispersion. *Nat. Commun.* **10**, 3930 (2019).

27. Bachtold, A., Moser, J. & Dykman, M. Mesoscopic physics of nanomechanical systems. *Rev. Mod. Phys.* **94**, 045005 (2022).

28. Micchi, G., Avriller, R. & Pistolesi, F. Mechanical signatures of the current blockade instability in suspended carbon nanotubes. *Phys. Rev. Lett.* **115**, 206802 (2015).

29. Knobel, R. G. & Cleland, A. N. Nanometre-scale displacement sensing using a single electron transistor. *Nature* **424**, 291–293 (2003).

30. Lassagne, B., Tarakanov, Y., Kinaret, J., Garcia-Sanchez, D. & Bachtold, A. Coupling mechanics to charge transport in carbon nanotube mechanical resonators. *Science* **325**, 1107–1110 (2009).

31. Steele, G. A. et al. Strong coupling between single-electron tunneling and nanomechanical motion. *Science* **325**, 1103–1107 (2009).

32. Okazaki, Y., Mahboob, I., Onomitsu, K., Sasaki, S. & Yamaguchi, H. Gate-controlled electromechanical backaction induced by a quantum dot. *Nat. Commun.* **7**, 11132 (2016).

33. Khivrich, I., Clerk, A. A. & Ilani, S. Nanomechanical pump–probe measurements of insulating electronic states in a carbon nanotube. *Nat. Nanotechnol.* **14**, 161–167 (2019).

34. Urgell, C. et al. Cooling and self-oscillation in a nanotube electromechanical resonator. *Nat. Phys.* **16**, 32–37 (2020).

35. Wen, Y. et al. A coherent nanomechanical oscillator driven by single-electron tunnelling. *Nat. Phys.* **16**, 75–82 (2020).

36. Blien, S., Steger, P., Hüttner, N., Graaf, R. & Hüttel, A. K. Quantum capacitance mediated carbon nanotube optomechanics. *Nat. Commun.* **11**, 1636 (2020).

37. Vigneau, F. et al. Ultrastrong coupling between electron tunneling and mechanical motion. *Phys. Rev. Research* **4**, 043168 (2022).

38. Gardner, J., Bennett, S. D. & Clerk, A. A. Mechanically probing coherent tunneling in a double quantum dot. *Phys. Rev. B* **84**, 205316 (2011).

39. Bhattacharya, U., Grass, T., Bachtold, A., Lewenstein, M. & Pistolesi, F. Phonon-induced pairing in quantum dot quantum simulator. *Nano Lett.* **21**, 9661–9667 (2021).

40. Samanta, C. et al. Nanomechanical vibrational response from electrical mixing measurements. Preprint at https://arxiv.org/abs/2207.02291 (2022).

Methods

Central theoretical results

We highlight the main theoretical results that emerge from the coupling of a nanomechanical resonator coupled to a quantum dot operated in the incoherent SET regime. When the vibrations are slow with respect to the typical electron tunnelling rate, one finds that the effective force reads as

$$F_{eff}(x) = -m\omega_m^{o\,2}x + F_e f_F(\epsilon - F_e x), \qquad (2)$$

where m is the eigenmode mass, ω_m^o is the bare resonance frequency, $F_e = \hbar g/x_{zp}$ is the variation in the force acting on the mechanical system when the number of electrons in the dot varies by one unit, ϵ is the electron energy level and f_F is the Fermi–Dirac function. One can define a resonance frequency from the quadratic term of the effective vibration potential obtained by the integration of F_{eff}. It reads $\omega_Q = \omega_m^o(1 - \epsilon_P/4k_B T)^{1/2}$, where $\epsilon_P = 2\hbar g^2/\omega_m^o$ is the polaronic energy, T is the temperature and k_B is the Boltzmann constant. Remarkably, the resonance frequency ω_Q associated with the linear restoring force decreases when lowering the temperature and vanishes at $T = 4\epsilon_P/k_B$. The dependence of ω_Q as a function of $\epsilon_P/k_B T$ is shown as a dotted (yellow) line in Extended Data Fig. 1.

Another striking effect of the coupling and of the suppression of ω_Q is that the nonlinear part of the restoring force becomes dominant at low temperatures. Due to this nonlinearity, the period of oscillation becomes strongly dependent on the oscillation amplitude. Thermal fluctuations allow the oscillator to explore different amplitudes and thus different resonance frequencies: when averaged, these fluctuations lead to an observed resonance frequency that is much higher than ω_Q (Extended Data Fig. 1, red line). In other words, the effect of nonlinearity becomes more important when the vibrations are cooled to a low temperature. This is just the opposite of what has been observed in mechanical resonators so far.

Despite the rich physics at work, the temperature dependence of the observed resonance frequency is a universal function of $\epsilon_P/k_B T$ for weak damping. We find this by calculating the displacement fluctuation spectrum $S_{xx}(\omega)$ (shown as a density plot; Extended Data Fig. 1). It has been shown[41] that $S_{xx}(\omega)$ is proportional to the amplitude response to a weak drive, which is what we measure in this work. The temperature dependence of the measured resonance frequency (Fig. 3d) agrees well with the prediction (Extended Data Fig. 1, full red line). It is used to extract the value of ϵ_P and therefore g.

Device production

Carbon nanotubes are grown on high-resistive silicon substrates with prefabricated platinum electrodes and trenches. The growth is done in the last step of the fabrication process to reduce surface contamination. Nanotubes are grown by the 'fast heating' chemical vapour deposition method, which comprises rapidly moving the sample from a position outside of the oven to the centre of the oven so that the temperature of the sample rapidly grows from room temperature to about 850 °C. This enables us to grow nanotubes over shallow trenches[42]. We remove the contamination molecules adsorbed on the nanotube surface during the transfer of the nanotube between the chemical vapour deposition oven and the cryostat, by applying a large current through the device under a ultrahigh vacuum at the base temperature of the dilution cryostat[43]. In the three measured devices, the nanotube–gate separation is 150 nm and the length of the suspended nanotube is between 1.2 and 1.4 μm.

Electrical characterization

We select ultraclean, small-bandgap semiconducting nanotubes. Extended Data Fig. 2a–c shows the charge stability diagram measurements at 6 K, 1 K and base temperature of the cryostat. The nanotube

regions in contact with the source and drain electrodes are p doped[44]. For large positive gate voltages, p–n junctions are formed along the nanotube near the metal electrodes, forming a quantum dot along the suspended nanotube. For gate voltage values below 0.05 V, the suspended nanotube region is p doped and the p–n junctions disappear, resulting in a higher conductance. The size of the Coulomb diamonds decreases as the number of electrons in the nanotube quantum dot increases. The charging energy E_c approximately varies from 8.5 to 6.5 meV in the gate voltage range discussed in the main text, whereas the level spacing ΔE changes from 0.97 to 0.73 meV. All the data shown in the main text and Supplementary Information are in the $k_B T < \Delta E, E_c$ regime. The short separation between the nanotube and gate electrode enables us to achieve a large capacitive coupling between the nanotube island and gate electrode as $C_g \gg C_s, C_d$, where C_s and C_d are the capacitances between the nanotube island and the source and drain electrodes, respectively. The diamonds in the charge stability diagram measurements become distorted when lowering the temperature due to the mechanical self-oscillations of the suspended nanotube generated at finite source bias voltages[31,34,35].

Temperature calibration

The temperature calibration in quantum dot devices operated in the incoherent SET regime ($\hbar\Gamma_e < k_B T < \Delta E, E_c$) is achieved by measuring the electrical conductance peak (Extended Data Fig. 3a), where Γ_e is the electron coupling rate and T is the temperature. The electron temperature is obtained from the width of the gate voltage V_g^{dc} of the conductance peak using the standard incoherent SET description (Supplementary Equation (5)):

$$G = \frac{G_0}{\cosh^2\left[\alpha(V_g^{dc} - V_P)/2k_B T\right]}. \qquad (3)$$

Here G_0 is the T-dependent peak conductance, α is the lever arm and V_P is the gate voltage of the conductance peak. We checked with the numerical calculations of the Fokker–Planck equation that the modification of the width of the conductance peak by electromechanical coupling is negligible over the measured temperature range. Extended Data Fig. 3b shows that the electron temperature is linear with the cryostat temperature except at low temperatures where it saturates at about 100 mK.

We cannot estimate the temperature of mechanical vibration fluctuations by measuring their spectrum as a function of temperature, since the low mechanical quality factor due to electron tunnelling in the SET regime impedes us to resolve the resonance of thermal vibrations. In another work[34], we measured the vibration fluctuation temperature of a high-quality-factor nanotube device as a function of cryostat temperature using the same cryostat and the same cabling, filters and amplifier; we observed that the vibration temperature is linear with the cryostat temperature down to a saturation temperature that is similar to the electron saturation temperature (Extended Data Fig. 3b). This indicates that the vibration temperature and electron temperature are similar.

Data availability

Source data are available for this paper. All other data that support the plots within this paper and other findings of this study are available from the corresponding author upon reasonable request.

References

41. Micchi, G., Avriller, R. & Pistolesi, F. Mechanical signatures of the current blockade instability in suspended carbon nanotubes. *Phys. Rev. Lett.* **115**, 206802 (2015).
42. de Bonis, S. L. et al. Ultrasensitive displacement noise measurement of carbon nanotube mechanical resonators. *Nano Lett.* **18**, 5324–5328 (2018).

43. Yang, W. et al. Fabry-Pérot oscillations in correlated carbon nanotubes. *Phys. Rev. Lett.* **125**, 187701 (2020).
44. Laird, E. A. et al. Quantum transport in carbon nanotubes. *Rev. Mod. Phys.* **87**, 703–764 (2015).

Acknowledgements

Author contributions

C.S., S.L.D.B. and D.A.C. fabricated the devices with contributions from B.S. and B.T. C.S. and S.L.D.B. carried out the measurements with support from C.B.M., R.T.-Q., W.Y. and C.U. Y.J. provided the amplifier used in the measurements. F.P. developed the theory. C.S., S.L.D.B., F.P. and A.B. analysed the data. C.S., C.B.M., D.A.C., F.P. and A.B. wrote the manuscript with inputs from the other authors. A.B. supervised the work.

Competing interests

The authors declare no competing interests.

Additional information

Extended data is available for this paper at https://doi.org/10.1038/s41567-023-02065-9.

Supplementary information The online version contains supplementary material available at https://doi.org/10.1038/s41567-023-02065-9.

Correspondence and requests for materials should be addressed to A. Bachtold.

Peer review information *Nature Physics* thanks Shabir Barzanjeh and the other, anonymous, reviewer(s) for their contribution to the peer review of this work.

**Reprints and permissions information** is available at www.nature.com/reprints.
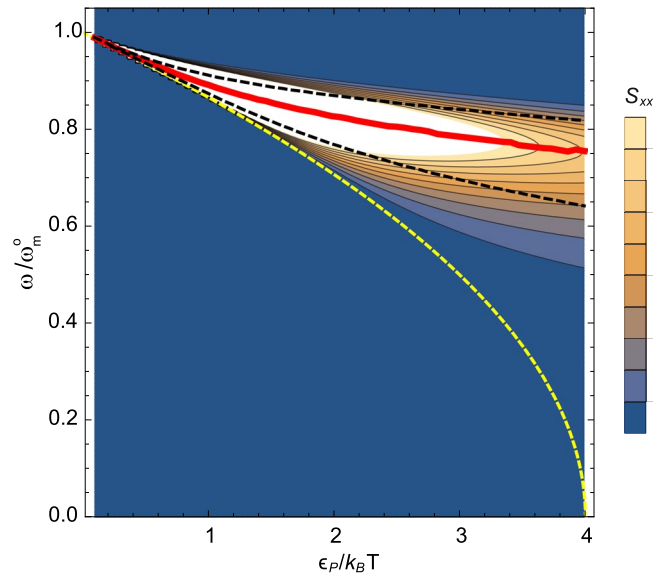
Extended Data Fig. 1 | Universal behavior of the temperature dependence of the resonance frequency expected by theory. Contour plot on the plane $\epsilon_P/k_B T - \omega$ of the intensity of the spectrum $S_{xx}(\omega)$ in units of $\epsilon_P/m\omega_0^3$. The spectrum is evaluated at a conductance peak; this is the well-known peak arising from single-electron tunneling in quantum dots as the gate voltage is swept. The thick continuous red line indicates the maximum of the spectrum, the dashed black lines indicates the values ω for which the intensity of the spectrum is reduced by a factor of 2 with respect to the maximum. The yellow dotted line is the prediction of Supplementary Equation 35 for the value of ω_Q.
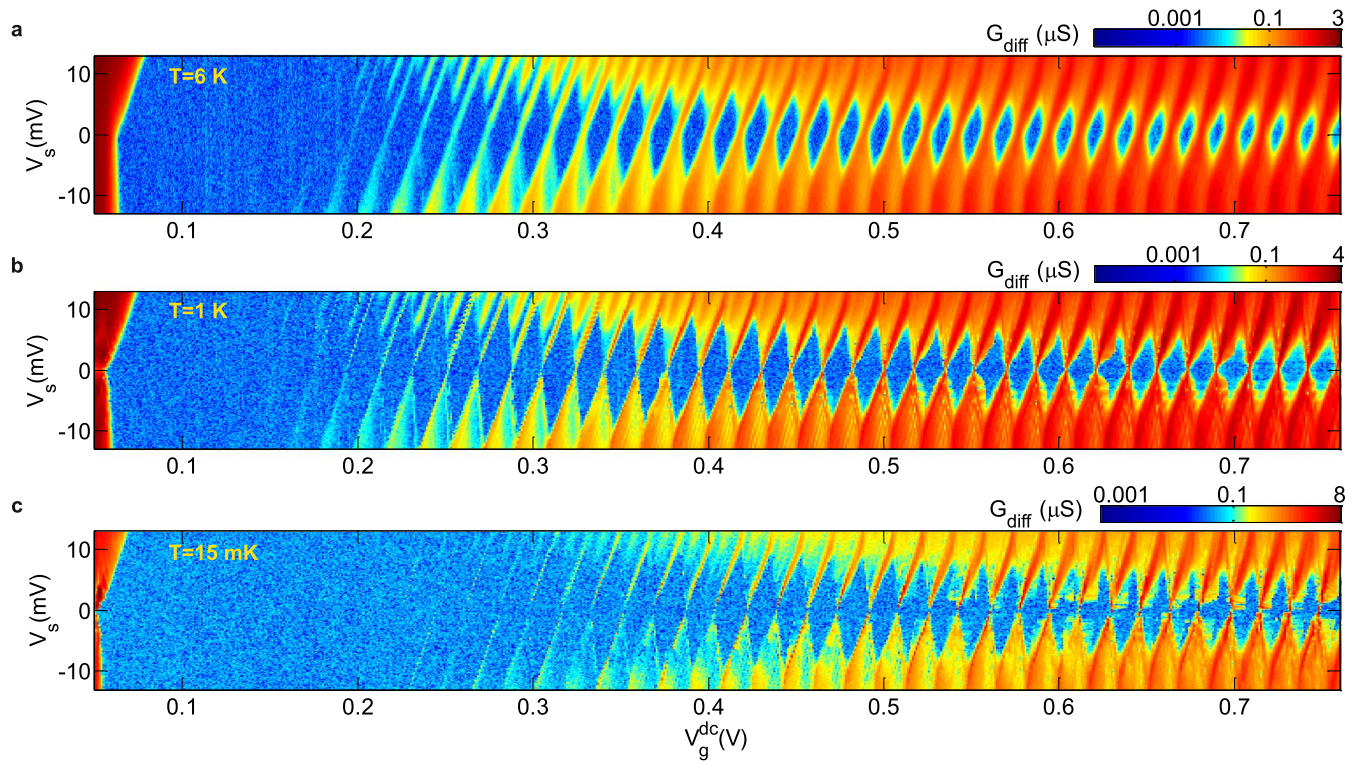
Extended Data Fig. 2 | Charge stability diagram measurements at different temperatures. Differential conductance of device I measured as a function of the source-drain voltage Vs and the gate voltage V_g^{dc} at different temperatures. The temperature of the cryostat is (a) 6 K, (b) 1 K, and (c) 15 mK.

a

b
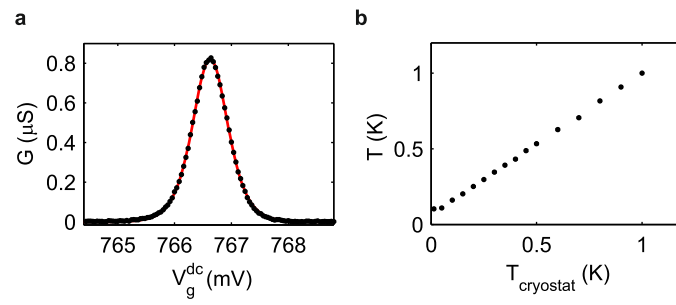
Extended Data Fig. 3 | Temperature calibration. (a) Gate voltage dependence of the conductance of device I at T = 1 K. The red solid line is the fit to the data using Eq. (3). (b) The electron temperature of the device measured as a function of the cryostat temperature.